Probing the Assembly History of Early−Type Galaxies

Principal Investigator: Daniel A. Dale

Institution: University of Wyoming

Electronic mail: ddale@uwyo.edu

Technical Contact: Daniel A. Dale, University of Wyoming

Co−Investigators: Liese van Zee, Indiana University

Shawn Staudaher, University of Wyoming

Kate Barnes, Indiana University

Robert Feldmann, University of California at Berkeley

Science Category: Extragalactic: nearby galaxies (z<0.05, v_sys<15,000 km/s)

Observing Modes: IRAC Post−Cryo Mapping

Hours Requested: 777.7

Proprietary Period(days): 0

Abstract:
Elliptical and S0 galaxies are thought to arise from a complex history of merger events. Since such systems are typically old and largely devoid of gas, the optimal tracer for revealing this merger history is the distributions of their older stellar populations. We propose to obtain extremely deep observations of a complete sample of early−type galaxies within 35 Mpc. The main goal of the survey is to quantify the morphological differences in the stellar populations as a function of environment, from the cores of galaxy clusters to the field. With sensitivity to tidal features and substructures with stellar mass surface densities less than 0.1 Msun/pc^2, this project will complement a similar survey of extended structures in spiral galaxies.

1 Science Plan

1.1 Science Justification

In the hierarchical view of the Universe, elliptical galaxies are formed through mergers between galaxies and the accretion of satellite galaxies. In clusters of galaxies, where elliptical and S0 galaxies are prevalent, additional dynamical interactions can impact galaxy stellar and gas morphologies. High speed close encounters ("galaxy harassment"), ram pressure stripping, and galaxy-cluster tidal interactions can all serve to modify the appearance of cluster galaxies, and the ensuing debris may take the form of striking stellar and/or HI tails, streamers, shells, and broad plumes (Gunn & Gott 1972; Dressler 1984; Byrd & Valtonen 1990; Mihos 1995; Moore et al. 1996; Dale et al. 2001; Conselice 2006). Over time individual stars within these features will either fall back to their parent galaxies or merge with the intracluster medium. Efforts to observationally quantify this diffuse "intracluster light" have proved challenging, with claims of detections occuring at or near the limits of available technology (e.g., Mihos et al. 2005; Rudick et al. 2010; Krick et al. 2011). An alternative method for constraining the merger history of early-type galaxies is to search for and characterize the properties of the tidal features themselves and the irregular morphologies in general that may be leftover from previous interactions (Chonis et al. 2011; Duc et al. 2011; Martínez-Delgado et al. 2012). Recent work indicates the presence of such features in over 70% of early-type galaxies (van Dokkum 2005; Tal et al. 2009).

The evidence and frequency of tidal features should be reflected in the environments in which galaxies reside, but it remains unclear exactly how the dependence on environment should manifest itself. For example, if massive ellipticals near the cores of dense clusters of galaxies are the end products of multiple major mergers, one may naively think they should exhibit the most prominent and greatest number of tidal features. However, two factors work against this assumption: the merger rate per galaxy in dense clusters is relatively low due to the high velocity dispersions for massive clusters, and any signs of previous interactions may be quickly erased given the frequency of (non-merger) galaxy-galaxy interactions in such dense environments. On the other hand, early-type galaxies found in the field outside of clusters likely have undergone fewer galaxy-galaxy interactions, but the evidence for such interactions is less likely to be subsequently eroded given the dearth of neighboring systems. This line of reasoning can likewise be extended to early-type galaxies found in groups, where both the galactic densities and the potential for the erasure of tidal features are intermediate compared to the cluster and field environments.

With this project we propose to observe a large unbiased and volume-limited sample of nearby early-type galaxies residing in a wide range of environments to statistically quantify the presence and amplitude of tidal features. *The proximity and environmental breadth of the sample in conjunction with Spitzer's unprecedented near-infrared surface brightness sensitivity, at precisely the wavelengths over which the emission from old stars in early-type galaxies peak, will provide a characterization of the merger history of early-type galaxies that is unmatched by any ground-based campaign.* The following sections provide details on particular science applications.

1.1.1 Observations Plus Simulations: Constraining Merger Histories

As described above, many galaxies show tidal tails, loops, shells, or isophotal disturbances when observed at low surface brightness levels (e.g., Arp 1966; Schweizer 1980; Schweizer

1982; van Dokkum 2005). Toomre (1972) demonstrated in a seminal work that such features are the tidal signatures of close encounters / mergers between galaxies. Since then the analysis of the origin, structure, and kinematic properties of tidal features and the fate of the galaxy merger product has been guided to a large degree by numerical simulations of ever increasing realism and resolution (e.g., White 1978, 1979; Farouki & Shapiro 1982; Barnes 1988, 1992; Hernquist 1992; Hernquist 1993; Hibbard & Mihos 1995; Combes et al. 1995; Barnes & Hernquist 1996; Springel & White 1999; Nipoti et al. 2003; Naab & Burkert 2003; Naab et al. 2006; Cox et al. 2006; Di Matteo et al. 2007; Di Matteo et al. 2008; Feldmann et al. 2008; Teyssier et al. 2010; Moster et al. 2011; Bois et al. 2011; Duc et al. 2011; Hopkins et al. 2013; Karl et al. 2013).

For instance, shells observed in the outer regions of many nearby elliptical galaxies are now understood as the post-merger phase-wrapped material from a spatially compact or kinematically cold stellar system and occur under relatively generic conditions (Quinn 1984; Hernquist & Quinn 1988). In contrast, the properties of prominent tidal tails and loops are closely related to the structural and kinematic properties of the merging system (Springel & White 1999; Feldmann et al. 2008; Duc et al. 2011; Wang et al. 2012). In several cases numerical simulations enabled detailed reconstructions of the orbits and properties of the merger progenitors, such as for NGC 4038/NGC 4039 Antennae system (Barnes 1988; Teyssier et al. 2010; Karl et al. 2013). Numerical simulations are also the method of choice for determining the observational lifetimes of the various features (e.g., Feldmann et al. 2008). When put in a cosmological context such studies allow us to connect the observed tidal features with the role of major and minor mergers in the assembly history of galaxies and with the morphological mix of the galaxy population.

The large sample size and imaging depth of the proposed project will enable us to perform a unique study of the recent ($\sim$ 1 Gyr ago) assembly history of early-type galaxies in both the field and the cluster environment. In order to interpret the observational findings we plan to analyze the origin of the observed tidal disturbances with the help of high resolution numerical simulations. Specifically, *we intend to extract the various properties of the merger/interaction progenitors, such as their masses, morphological types, and orbits as a function of environment. Based on these results we aim to quantify the importance of environment and the role of recent major and minor merging in the assembly history of early-type galaxies.* Focussing on the differences between these extreme environments will help in reducing potential systematics in our analysis. We will also compare our findings with those inferred directly from the galaxy mass function and the morphology-density relation.

1.1.2 Formation of S0 Galaxies

S0, or lenticular, galaxies are noted for their thick, featureless disks that are largely devoid of interstellar gas and active star formation as well as their relatively prominent, aged bulges. From a morphological viewpoint they are intermediate between spiral galaxies and ellipticals. In spectral terms they share many common features with elliptical galaxies. This interesting mix of properties naturally leads to questions about the origin of S0 galaxies. Are they former elliptical galaxies that later grew a disk, are they faded former disk galaxies that lost their gas-rich envelopes and subsequently added a strong bulge, or is there another explanation for their provenance (Larson et al. 1980)? Numerical simulations show that galaxy harassment, tidal interactions, and stellar evolution can all lead to a thickening of the stellar disk and a prominent bulge, and ram pressure/viscous stripping will quickly starve S0 systems in

galaxy clusters of the fuel necessary for any significant future star formation (Quilis et al. 2000). The rise of field S0s is less easily prescribed. To help answer these questions, various observational programs have been carried out to track galaxy morphologies over time. Early studies showed that the fraction of elliptical and S0 galaxies is higher in denser environments (Dressler 1980), and that this fraction seems to change as a function of redshift (Butcher & Oelmer 1984; Dressler & Gunn 1992). More recent efforts based on high angular resolution HST imaging have apparently provided direct evidence for smaller percentages of lenticulars in clusters at redshifts higher than $z \sim 0.4$, suggesting that S0s form later than ellipticals and such formation occurs over shorter timescales (Dressler et al. 1997; Fasano et al. 2000; Smith et al. 2005; Postman et al. 2005; Poggianti et al. 2006; Desai et al. 2007; Wilman et al. 2009).

However, these claims have recently been challenged: Holden et al. (2009) suggest that, after properly accounting for the artificial increase (or "blurring") in observed ellipticities at higher redshifts, the fractional population of early-type galaxies is unchanged from that observed in the present epoch. *Our proposed observations will help to shed light on this quandary of the origin of S0 galaxies by constraining the formation histories of both elliptical and S0 galaxies over a wide range of environments, from the core of the Virgo Cluster to isolated galaxies in the field.*

1.1.3 Stellar Cluster Populations in the Outskirts of Early-Type Galaxies

In addition to extended stellar features, we will detect both young and old star clusters associated with the host galaxies. Indeed, we expect to find a large distribution of globular clusters around most galaxies, with particularly extended distributions in fields containing pure elliptical galaxies. We will therefore extract a point source catalog for every field. While we expect the majority of star clusters in the outskirts of these galaxies to be old, these near-infrared data will be combined with available multi-wavelength data (GALEX UV for all the galaxies and SDSS for half the sample) to carry out spectral energy distribution fitting to estimate cluster properties such as age, mass, and extinction (e.g., Dong et al. 2008; Alberts et al. 2011). The near-infrared fluxes from *Spitzer* 3.6 and 4.5 μm imaging observations are crucial to our efforts to disentangle age-metallicity-extinction degeneracies for each candidate star cluster (e.g., Spitler et al. 2008).

The combined point source catalog for all of the galaxies in the survey will provide a unique opportunity to examine the processes associated with globular cluster formation and evolution. In particular, the well known optical color bimodality of globular clusters has long been interpreted as a metallicity bimodality (e.g., Brodie & Strader 2006, and references therein) with the corresponding conclusion that there must be at least two major epochs of globular cluster formation in the host galaxy. However, these conclusions can be difficult to reconcile in a hierarchical merging scenario where globular clusters are formed during multiple merging events. Indeed, while it is possible to form a bimodal metallicity distribution in hierarchical galaxy formation simulations (e.g., Muratov & Gnedin 2010), it requires additional tuning of the parameters and late stage massive merger events. Alternative interpretations of the optical color bimodality have been suggested and include the recognition that a unimodal metallicity distribution can appear as a bimodal optical color distribution if the horizontal branch morphology has a non-linear color-metallicity relation (e.g., Yoon et al. 2006). However, the combination of optical/near-IR colors are much less sensitive to this effect (e.g., Cantiello & Blakeslee 2007). Thus, the proposed observations will

help break the age-metallicity degeneracy for a large statistical sample of globular clusters around early-type galaxies and, in combination with existing optical data on these systems, will provide an excellent test of globular cluster formation mechanisms.

Furthermore, *the proposed wide-field observations will allow us to determine, for the first time, the shape of the cluster mass function in these extremely low surface density regions*, which can then be compared with the typical power-law mass function ($\psi(M) \propto M^{\beta}$, with $\beta \sim -2$) observed for clusters formed within the optically luminous portions of star-forming galaxies (e.g., Fall et al. 2009; Chandar et al. 2010a,b; Cook et al. 2012). The masses and ages of the clusters will also allow us to assess the ability of star clusters to remain gravitationally bound in the outskirts of early-type galaxies. These results will be compared with those found in the main bodies of galaxies (e.g., Fall et al. 2005; Bastian et al. 2012) to determine whether similar physical processes dominate in different galaxy environments.

1.1.4 The Structure of Early-Type Galaxies

Although our main scientific emphasis is on detecting and characterizing the low density stellar plumes and tidal streamers as a function of galaxy environment, our proposed observations will also yield superb information on the two-dimensional distribution of stellar light within the main bodies of our target galaxies. The near-infrared emission will probe the low mass stellar populations, and thus be directly proportional to the stellar mass, irrespective of the star formation history. With our stellar maps, we will measure both axisymmetric and non-axisymmetric structural parameters. These parameters are important probes of a particular galaxy's dynamical history (Buta et al. 2004), and quantifying them across a large unbiased and volume-limited sample of elliptical and S0 will be pivotal to understanding galaxy evolution and the formation of the Hubble sequence (Kormendy & Kennicutt 2004). For example, Gu et al. (2013) use the residual shells left after subtracting models based on isophotal ellipse fitting to constrain the merger history of the central cD galaxy of the Coma cluster. Huang et al. (2013) similarly utilize optical imaging in conjunction with 2D isophotal analysis and the resulting substructures to investigate the formation history of a sample of 94 massive ellipticals.

The depth of our near-infrared imaging will also allow us to search for correlations between the easily-measured high surface brightness features and the faint structures seen in the outskirts. This comparison may allow us to link the dynamical evolution of the inner and outer regions, especially interesting if isophotal "twists" persist over large scales. Finally, with the planned surface brightness sensitivity it may be possible to connect the slopes of the outer isophotal profiles to the observed spatial distributions of the globular cluster candidates.

The proposed observations, with their unprecedented surface brightness sensitivity to extended distributions of old stars, will therefore provide a unique data set on the stellar mass distributions associated with early-type galaxies, at wavelengths that are insensitive to both dust extinction and the galaxy's star formation history. *In combination with the EDGES Survey on spiral galaxies (completed in Cycle 8), these observations provide an unbiased view of the stellar population of galaxies in a range of environments in the nearby universe and therefore provide unique insight into galaxy formation and evolution in a ΛCDM Universe.*

1.1.5 Why *Spitzer*?

The light from early-type galaxies is dominated by old stars whose emission peaks in the near-infrared, and thus near-infrared imaging is an ideal approach to mapping out the tidal features associated with early-type galaxies. However, there are relatively few wide-field near-infrared imagers available to the general astronomical community. Moreover, ground-based observations of low surface brightness features are technically challenging at any wavelength (see, e.g., Martínez-Delgado et al. 2009), but particularly in the near-infrared. The systematic and technical difficulties produced by generally variable sky levels in the near-infrared lead to ground-based *surface brightness* sensitivities that are significantly inferior to what is possible with *Spitzer*. For example, our 1800 s integration Cycle 8 data provide an effective limiting surface brightness sensitivity of 0.2 kJy sr^{-1} (1σ AB of 30 mag arcsec^{-2}; see § 1.2.2 and Figure 2). An integration that is ten times as long (4.9 hr) using the new FourStar imager on the Baade 6.5 m Magellan telescope, in contrast, only probes down $K_s =18$ kJy sr^{-1} (AB of 25 mag arcsec^{-2}) averaged over arcminute scales (Persson et al. 2013; Ivo Labbé, private communication). The UKIDSS Ultra-Deep Survey provides another ground-based comparison (Lawrence et al. 2007). Inspection of their publicly-available DR8 K-band image ($T \sim 50$ hr on a 3.8 m telescope) suggests a 1σ limit over arcminute scales of 8 kJy sr^{-1} (AB of 26 mag arcsec^{-2}).

In light of these difficulties with ground-based near-infrared imaging, an alternative method for detecting faint streamers is to stack ground-based optical data from multiple broadband filters or utilize a single extremely wide filter. van Dokkum (2005) obtains 28 mag arcsec^{-2} after stacking 8 hour B, V, and R data from 4 m telescopes. It is an ambitious task to detect faint streamers and plumes with this sensitivity, since the older/redder features appear below 27 mag arcsec^{-2} (e.g., Duc et al. 2011). Martínez-Delgado and collaborators take a conceptually similar but technically different approach and utilize a filter that spans 3500-8500Å (Martínez-Delgado et al. 2009; 2010; 2012; Chonis et al. 2011). After stacking up to tens of hours of ground-based optical data taken with more modest size telescopes, they achieve a similar surface brightness sensitivity as van Dokkum and co-workers. It is difficult to go any deeper than this from the ground in terms of surface brightness, as large-scale flat-fielding residuals/internal reflections/ghosts/scattered light/etc. play more important roles than photon noise for extremely long integrations (e.g., § 2.4 of Tal et al. 2009 and § 2 of Martínez-Delgado et al. 2010). Moreover, in addition to such technical demands with imaging systematics, the photometric calibration and subsequent analysis via such unique approaches can be challenging.

1.2 Technical Justification

1.2.1 Sample Definition

The volume-limited parent sample for this work derives from all 1076 2MASS galaxies out to $cz < 2500$ km s^{-1} that satisfy $M_{K_s} < -21.5$ mag, which is the limiting absolute magnitude at the volume's edge ($D = 35.2$ Mpc) for a limiting apparent magnitude of $m_{K_s} = 11.25$ mag. A K_s apparent magnitude of 11.25 is two magnitudes brighter than the 90% completeness limit for 2MASS extended sources more than 30° above the Galactic plane (see Section 5.3 and Figure 23 of Skrutskie et al. 2006). We select from this database all 155 early-type galaxies ($T \leq 0$) that lie at high Galactic latitudes ($|b| > 60°$) in order to avoid undue contamination by foreground Milky Way stars.

To quantify the range of environments in which these 155 early-type galaxies reside, we compute for each system an adaptive density metric

$$\rho_{10} = N_{\mathrm{gal}}/(4/3\pi R_{10}^3) \tag{1}$$

where R_{10} is the distance to the tenth nearest neighbor (i.e., $N_{\mathrm{gal}} = 10$ and excludes the galaxy in question). Such volumetric number densities were first described in Dressler (1980) and recently refined in Cappellari et al. (2011), for example. The computation involves first projecting each galaxy's coordinates and distance onto a three-dimensional Cartesian grid using distances obtained from the Extragalactic Distance Database (Tully et al. 2009). To avoid incompleteness issues in these computations at the outer $cz < 2500$ km s^{-1} edge of the volume surveyed, the densities for the members of both the early-type galaxy sample and the parent sample are computed using a larger reference sample that satisfies the same luminosity criterion but extends out to $cz < 3500$ km s^{-1}. See Figure 1 for the distributions of the early-type and parent galaxy samples in terms of local environment and color-magnitude.

1.2.2 Observing Plan

AORs are constructed using the successful strategy utilized for our Cycles 6 and 8 programs. Mosaics are built upon a grid of 100″ spacings (∼one-third the IRAC field of view). Two sets of maps will be obtained for each source to enable asteroid removal and data redundancy, and to build up the map sensitivity to the desired level. Thus, at any given location within the map cores there will be a total of 18 × 100 s frames resulting in a net integration per sky position of 1800 s (along with a ∼100″-wide "inner periphery" at a 1200 s integration and a ∼100″-wide "outer periphery" at 600 s).

Inspection of our Cycle 8 data on a sample of 92 spiral galaxies shows some 3.6 μm tidal features extending to ∼ $3R_{25}$. Our proposed 3.6 μm observations are thus designed to map 1800 s core regions out to at least $3R_{25}$ (Figure 3). The smallest maps will be 6x6 mosaics, ensuring at least 6.7′ map cores at the deepest $T = 1800$ s effective integration and 10′ maps at $T \geq 1200$ s if the inner periphery is included. This will ensure enough coverage to adequately sample any extended stellar distributions while still allowing ample area for determining the sky value. Moreover, a 10′ map at the outer reaches of our sample (35 Mpc) spans 100 kpc, which is well matched to the ∼50 kpc maximum extent of tidal features in the van Dokkum (2005) ground-based study of 126 nearby red galaxies. We will center the mosaics for 3.6 μm observations; though the 4.5 μm mosaics will not be centered on the targets, they can be used for tidal feature confirmation where possible and provide the potential to trace the faint stellar population to even larger radii.

1.2.3 Planned Image Sensitivity

Our sample is restricted to galaxies with low infrared sky levels (median value of 120 kJy sr^{-1} at 3.6 μm), and thus we expect to achieve a 1σ noise level of 2 kJy sr^{-1} at 3.6 μm (based on our Cycles 6 and 8 data and on SENS-PET predictions). The simultaneous images at 4.5 μm will have a per pixel surface brightness sensitivity better than 3 kJy sr^{-1}.

These deep mosaics will trace the stellar distribution to unprecedented levels of less than 0.1 $M_\odot$ pc^{-2}, at wavelengths relatively insensitive to dust and star formation history. Indeed, the 1800 s integration per position would be much deeper than other surveys of nearby galaxies, e.g., SINGS ($N_{\rm gal} = 75; T$=240 s; Kennicutt et al. 2003), LVL ($N_{\rm gal} = 258; T$=240 s; Dale et al. 2009), S^{4}G ($N_{\rm gal} \sim 2300; T$=240 s; Sheth et al. 2010), and the IRAC GTO project ($N_{\rm gal} = 100; T$=60 or 150 s; Pahre et al. 2004). These surveys reach a 1σ sensitivity of a few to several kJy sr^{-1}, which is typically at the 5% level with respect to the near-IR sky surface brightness (Regan et al. 2006).

Analysis of our Cycle 8 data shows that averaging over just a few square arcminutes (e.g., azimuthal averaging) provides a 3.6 μm sensitivity of 0.2 kJy sr^{-1} (AB of 30 mag arcsec^{-2}), a level necessary for securing robust S/N for regions of faint stellar emission (see also Krick et al. 2011 for a similar sensitivity with ultra-deep Warm Spitzer imaging). For comparison, WISE achieves a 3.4 μm sensitivity larger than 1 kJy sr^{-1} over a 5$'$×5$'$ area (Wright et al. 2010). In terms of comparing to ground-based optical surveys, the proposed survey will be much more sensitive. Our effective sensitivity reaches two magnitudes deeper than that of van Dokkum and Martínez-Delgado and their respective co-workers, groups that utilize extremely wide filters or combine multiple broadband images into one very broad pseudo filter (see § 1.1.5 for more details).

1.2.4 Data Quality Control and AOR Efficiency

Approximately 10% of our Cycle 8 mosaics on nearby spirals involved saturated pixels near the galaxy cores, and another 30% showed evidence for non-linearities above a surface brightness of 30 MJy sr^{-1}. To remedy these issues we replaced the corrupted pixels using shorter exposure data from the ROC, where available. To ensure we do not likewise encounter saturation and/or non-linearities in the proposed program, which also utilizes 100 s exposures, we have added single 6 s AORs for the 14% of the proposed sample for which archival 3.6 μm data are unavailable. This safety precaution comes at a cost of only 2.5 hr, or 0.3% of our requested time budget, and it will allow for robust recovery of galaxy surface brightness profiles from their cores to their outer peripheries.

Several of the galaxies in our sample are projected to lie close in the sky to another galaxy in our sample. To maximize the efficient use of *Spitzer* time, for six such groups of galaxies we have combined neighboring/overlapping AORs into a single AOR. This economization results in a savings of 28 hr (3.6% in terms of the entire budget).

1.2.5 Data Processing

The post-pipeline processing of the data should be straightforward, given our substantial experience with SINGS, LVL, and Cycles 6 and 8 programs. The multi-epoch, multiple-pointing observations for each galaxy will be combined into a single mosaic for each band using the MOPEX mosaicking software. Additional post-BCD processing will include distortion corrections, rotation of the individual frames, bias structure and bias drift corrections,

column pulldown correction near bright sources, image offset determinations via pointing refinements from the SSC pipeline, detector artifact removal, constant-level sky subtraction, and image resampling to 0.75″ pixels using drizzling techniques. The drizzling slightly improves the final PSF over the native one. We also correct for the so-called "clock time" effect and the "first frame" effect where there is a bias dependent on the delay time between exposures (see Krick et al. 2011).

The two largest challenges to measuring stellar emission in the extreme outer disks are the presence of foreground stars/background galaxies and the stability of the sky levels within the large maps. As explained above, we plan to minimize the first issue by constraining our sample to $|b| > 60°$. Furthermore, we have extensively explored how best to mask foreground stars and background galaxies. The optimal approach that we have converged upon relies on a multi-pronged strategy. We first carry out a by-eye masking of the brightest foreground stars and background galaxies. For detection purposes we employ Högbom CLEANing, which utilizes SSC-provided IRAC 2D PSFs to subtract off as much of the point sources as possible. After CLEANing we carry out a multi-resolution (wavelet) smoothing. Högbom CLEANing followed by wavelet-based smoothing helps to enhance the visibility of faint structures. Once identified, we prepare for photometry by using SExtractor (Bertin & Arnouts 1996) on the unsmoothed data with an empirical growth factor to mask the point source residuals.

To assess the sky stability, we have analyzed maps from our Cycles 6 and 8 programs executed at the same imaging depth. Inspection of our mosaics, which span scales as large as $\sim 1°$, shows sky variations less than 1 kJy sr^{-1}. We will map the entire field of view during each AOR (two per target), and thus changes across the field due to variations in zodiacal light will be minimized. In short, we have adopted our Cycles 6 and 8 mapping strategy for this proposal, and that strategy has proven successful for a similar set of goals.

1.2.6 Data Analysis

Tidal Features We will qualitatively examine the final mosaics and the resulting surface brightness profiles for evidence of extended plumes, streamers, and tidal features in general. The general prescription outlined in van Dokkum (2005) will be followed: 0 for no tidal features, 1 for weak features, 2 for strong features, and 3 for an ongoing merger. We will also quantitatively assess tidal features via measuring deviations from model emission profiles (van Dokkum 2005; Tal et al. 2009; Gu et al. 2013; Huang et al. 2013). The first step in such an analysis requires creating a model galaxy "M" by fitting isophotal ellipses to the observed emission (e.g., IRAF/`ellipse`), a process that can allow centroids, position angles, and ellipticities to vary with radius. A fractional distortion image "F" is computed by dividing the observed image "O" by the image of the model galaxy:

$$F = O/M. \tag{2}$$

A tidal parameter t_{tidal} quantifies the average deviation from the model, i.e.,

$$t_{\text{tidal}} = \overline{|F_{x,y} - \overline{F_{x,y}}|}, \tag{3}$$

and a version corrected for residual noise in the imaging has the form

$$t_{\text{tidal,cor}} = \sqrt{t_{\text{tidal}}^2 - t_{\text{tidal,model}}^2} \tag{4}$$

where $t_{\text{tidal,model}}$ is the tidal parameter extracted from the model galaxy M that has been added to a blank sky region of the image (see Tal et al. 2009, for example). This corrected

tidal feature parameter will be examined as a function of luminosity, color, and ρ_{10} (see Section 1.2.1), the latter in order to determine how the presence and strength of tidal features vary as a function of galaxy environment.

Surveying 155 early-type galaxies allows for a robust analysis of tidal feature data as a function of three separate parameters: luminosity, color, and environment. For example, a chi-square test (Press et al. 2007) could be used to test whether the population of field early-type galaxies have different corrected tidal parameters $t_{\mathrm{tidal,cor}}$ than the population of cluster early-type galaxies. If the $t_{\mathrm{tidal,cor}}$ data are binned into five bins for both the field and cluster galaxies, there would be $N_{\mathrm{total}}/N_{\mathrm{subpopulations}}/N_{\mathrm{bins}} = 155/2/5 \approx 15$ galaxies in each bin since there is a roughly equal split in our sample between the two populations (see Figure 1). Such binning would provide $\sim 25\%$ Poisson accuracy in each bin count ($\sqrt{15}/15 \sim 0.25$).

Stellar Masses The 3.6 μm data can be used to derive stellar masses of the tidal features. Johnston et al. (2001), for example, utilize a few assumptions on the dynamics of galaxy interactions and the observed tidal features to estimate the original stellar masses of satellites that are gravitationally drawn into a merger (see also Peñarrubia et al. 2005; Martínez-Delgado et al. 2009; Chonis et al. 2011). Another technique for estimating stellar mass simply relies on summing up the observed 3.6 μm emission and multiplying it by a canonical mass-to-light ratio for that wavelength. Initial analysis of our data for the M 63 stream (Figure 2) shows that these two techniques agree within 50% (i.e., $4 \cdot 10^8$ vs $6 \cdot 10^8$ $M_{\odot}$).

Numerical Simulations Numerical simulations will be utilized to interpret the observations (see § 1.1.1). A new or current graduate student will be recruited to work on this project at the University of Wyoming, where ample computational facilities are available including the 82-node Mt. Moran cluster and the NCAR-Wyoming Yellowstone supercomputer. The student would be jointly mentored by Dale and Feldmann.

Caveats to the Analysis Finally, the presence of 3.3 μm PAH emission in the IRAC1 band will likely be minimal due to the negligible dust present in galaxy outskirts (Gil de Paz et al. 2007b; Dong et al. 2008). Supporting this view is the low metallicity nature of galaxy peripheries ($Z/Z_{\odot} = 1/5 - 1/10$; Gil de Paz 2007b; Goddard et al. 2010b), coupled with the fact that low metallicity is known to depress PAH emission (e.g., Engelbracht et al. 2008; Muñoz-Mateos et al. 2009). Indeed, no extended ($\sim 2R_{25}$) PAH emission is seen in a limited study of one pointing in each of five spiral galaxies, with an imaging depth similar to that proposed here (Alberts et al. 2011).

1.2.7 Management Plan

PI Dale will coordinate the scientific efforts and management of the project and serve as Technical Contact. Data processing through mosaicking will be led by Staudaher, who has extensive experience from our Cycles 6 and 8 projects described in § 4. Barnes has developed expertise from past Warm Mission projects on the masking/cleaning of foreground Milky Way stars, and she will mentor UW and IU students on this task. van Zee will lead on comparisons to available Hı data. All team members will participate in the analysis of the data, and Feldmann will lead the comparison of observations to numerical simulations.
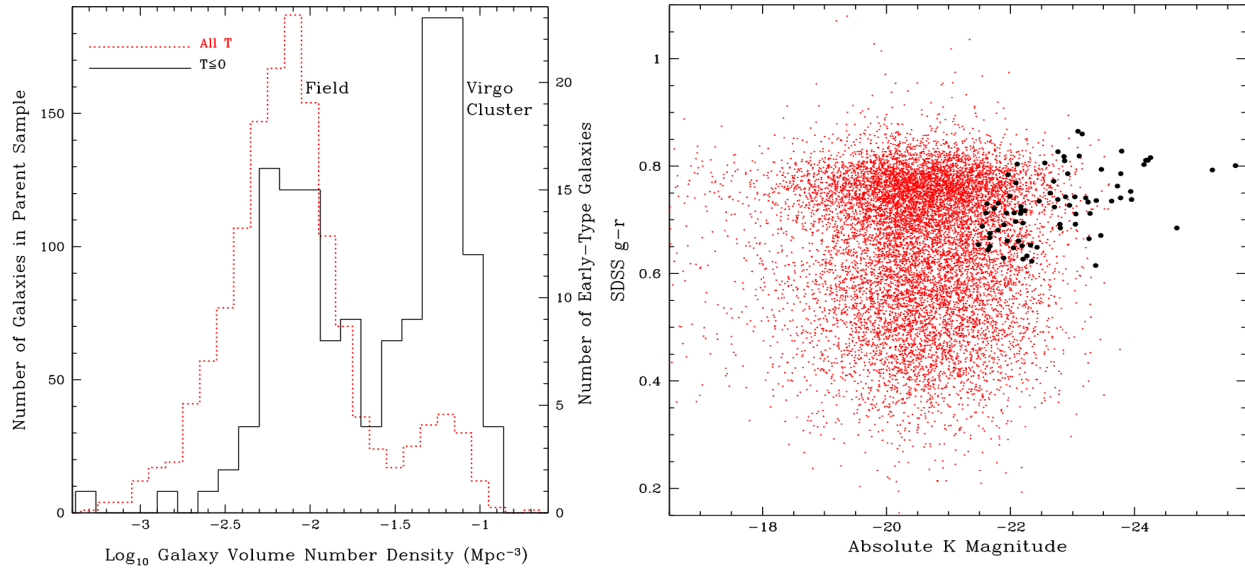
1.3 Figures, Tables & References

Figure 1: *Left*: Three dimensional volumetric number densities for both the parent sample (red dotted line) and the early-type galaxy sample (black line). The definition for ρ_{10} is provided in the text. *Right*: Color-magnitude relation for our early-type galaxy sample in addition to local galaxies (10–150 Mpc) from the NYU Value-Added Galaxy Catalog of SDSS systems in the local universe (Adelman-McCarthy et al. 2008; Blanton et al. 2005; Padmanabhan et al. 2008). Our sample of early-type galaxies has $g - r$ colors similar to that of the "red cloud", and is selected to follow $M_{K_s} < -21.5$ mag (§ 1.2.1).

References

Adelman-McCarthy, J.K. et al. 2008, ApJS, 175, 297

Alberts, S. et al. 2011, 731, 28

Arp, H. 1966, ApJS, 14, 1

Barnes, J. E. 1988, ApJ, 331, 699

Barnes, J. E. 1992, ApJ, 393, 484

Barnes, J. E., & Hernquist, L. 1996, ApJ, 471, 115

Bastian, N. et al. 2012, MNRAS, 419, 2606

Bertin, E. & Arnouts, S. 1996, A&AS, 117, 393

Blanton, M.R. et al. 2005, AJ, 129, 2562

Bois, M., Emsellem, E., Bournaud, F., et al. 2011, MNRAS, 416, 1654

Brodie, J. P., & Strader, J. 2006, ARA&A, 44, 193

Butcher, H. & Oelmer, A. 194, ApJ, 285, 426

Byrd, G. & Valtonen, M. 1990, ApJ, 350, 89

Cantiello, M. & Blakeslee, J. P. 2007, ApJ, 669, 982

Cappellari, M. et al. 2011, MNRAS, 416, 1680

Chandar, R. 2010a, ApJ, 713, 134

Chandar, R. 2010b, ApJ, 719, 966

Chonis, T.S. et al. 2011, AJ, 142, 166

Combes, F., Rampazzo, R., Bonfanti, P. P., Prugniel, P., & Sulentic, J. W. 1995, A&A, 297, 37

Conselice, C.J. 2006, ApJ, 638, 686

Cook, D.O. et al. 2012, ApJ, 751, 100

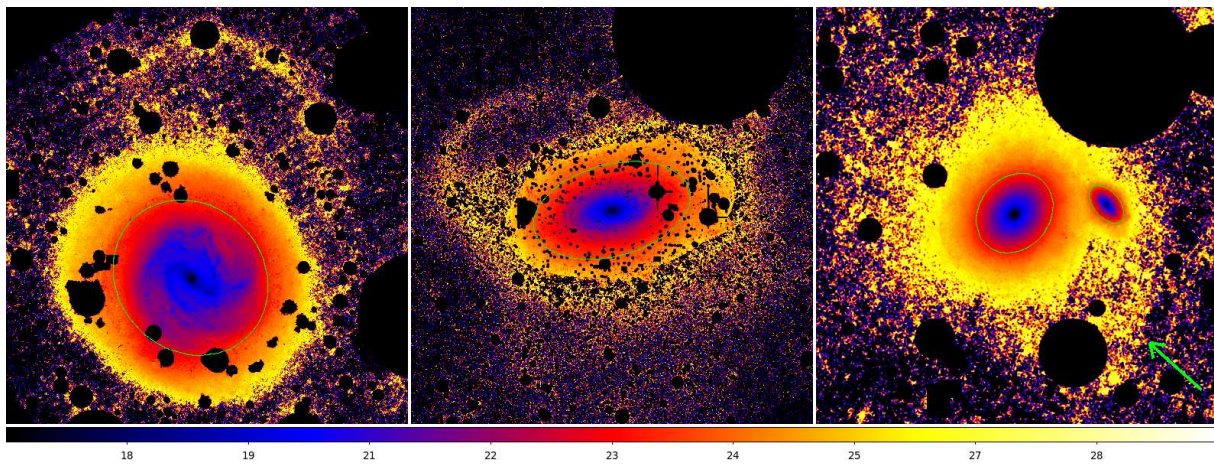Cox, T. J., Dutta, S. N., Di Matteo, T., et al. 2006, ApJ, 650, 791

Figure 2: Zoomed-in views of our deep 3.6 μm mosaics of M 83 (left; 30$'$) and M 63 (middle; 30$'$) and NGC 3998 (right; 13$'$), exemplifying the ability of the proposed observational scheme to detect faint tidal features in nearby galaxies. The streams have surface brightnesses of 3-5 kJy sr^{-1} ($\sim$26.7-26.2 mag arcsec^{-2} AB), whereas our effective sensitivity is 0.2 kJy sr^{-1} ($\sim$30 mag arcsec^{-2}). See also Figure 3. The tidal feature associated with M 83, also known as *[KK98]208, was targeted in the LVL survey (Dale et al. 2009) but was not detected via that survey's 240 s-depth imaging program.* The RC3 $a_{25} \times b_{25}$ ellipses are shown in green, including for the companion galaxy NGC 3990 in the righthand panel.

Dale, D.A. et al. 2001, AJ, 121, 1886

Dale, D.A. et al. 2009, ApJ, 703, 517

Delaye, L. et al. 2013, MNRAS, submitted

Desai, V. et al. 2007, 660, 1151

Di Matteo, P., Combes, F., Melchior, A.-L., & Semelin, B. 2007, A&A, 468, 61

Di Matteo, P., Bournaud, F., Martig, M., et al. 2008, A&A, 492, 31

Dong, H., Calzetti, D., Regan, M., Thilker, D., Bianchi, L., Meurer, G.R., & Walter, F. 2008, AJ, 136, 479

Dressler, A. 1980, ApJ, 236, 351

Dressler, A. 1984, ARAA, 22, 185

Dressler, A. & Gunn, J.E. 1992, ApJS, 78, 1

Dressler, A. et al. 1997, ApJ, 490, 577

Dubinski, J., Mihos, J. C., & Hernquist, L. 1996, ApJ, 462, 576

Duc, P.-A., Cuillandre, J.-C., Serra, P., et al. 2011, MNRAS, 417, 863

Engelbracht, C. et al. 2008, ApJ, 678, 804

Fall, S.M. et al. 2005, ApJL, 631, L133

Fall, S.M. et al. 2009, ApJ, 704, 453

Farouki, R. T., & Shapiro, S. L. 1982, ApJ, 259, 103

Fasano, G. et al. 2000, ApJ, 542, 673

Feldmann, R., Mayer, L., & Carollo, C. M. 2008, ApJ, 684, 1062

Gil de Paz, A. et al. 2007b, ApJ, 662, 115

Goddard, Q.E., Kennicutt, R.C., & Ryan-Weber, E.V. 2010, MNRAS, 405, 2791

Gu, M. et al. 2013, ApJ, in press

Gunn, J.E. & Gott, J.R.I. 1972, ApJ, 176, 1

Hernquist, L., & Quinn, P. J. 1988, ApJ, 331, 682

Hernquist, L. 1992, ApJ, 400, 460

Hernquist, L. 1993, ApJ, 409, 548

Hibbard, J. E., & Mihos, J. C. 1995, AJ, 110, 140
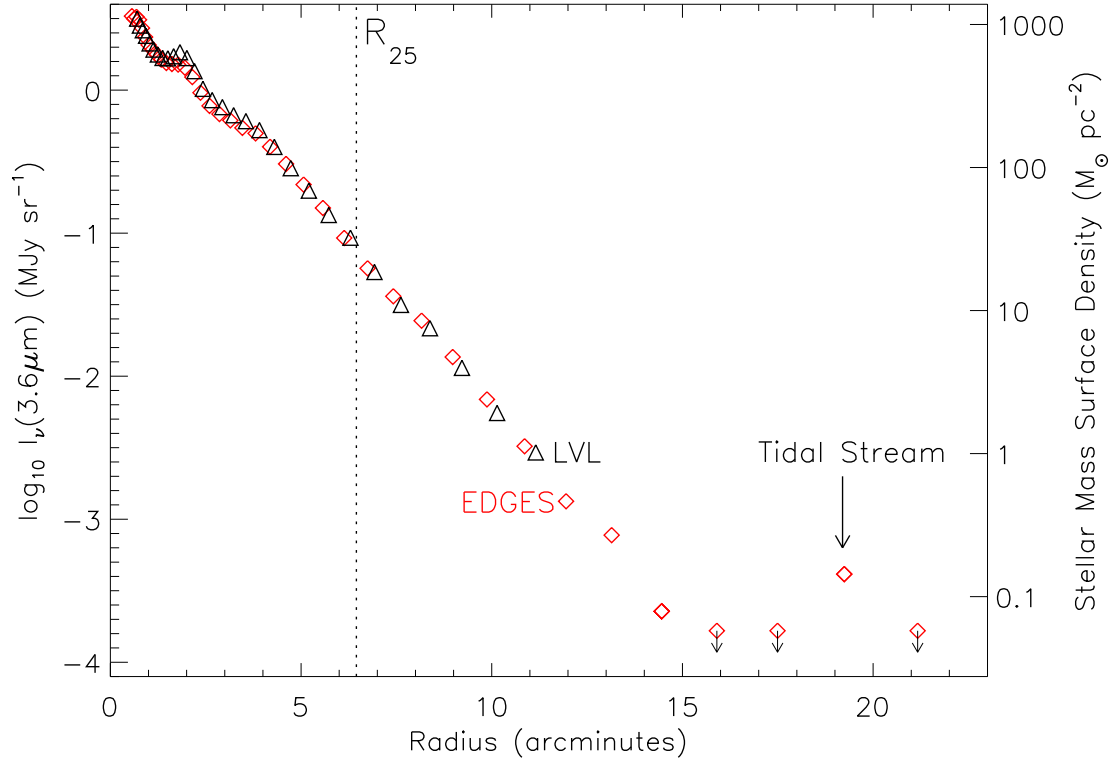
Figure 3: Results from LVL (240 s integration per pixel; Dale et al. 2009) and our Cycle 6 program (1800 s per pixel) for M 83. The LVL observational scheme (which is the same used in the SINGS and S^{4}G surveys) is not sensitive enough to detect the tidal stream associated with M 83. The stellar mass surface density quantified along the righthand axis assumes $M/L \sim 0.5 M_\odot/L_\odot$, based on a rotation curve decomposition (Barnes et al. 2013, in prep.). *Our deep Spitzer observations allow us to quantify the stellar surface mass density and the total stellar mass associated with this stream for the first time.*

Holden, B.P. et al. 2009, ApJ, 693, 617

Hopkins, P. F., Cox, T. J., Hernquist, L., et al. 2013, MNRAS, 430, 1901

Huang, S. et al. 2013, ApJ, 766, 47

Johnston, K.V. et al. 2001, ApJ, 557, 137

Karl, S. J., Lunttila, T., Naab, T., et al. 2013, arXiv:1305.0828

Kennicutt, R.C. et al. 2003, PASP, 115, 928

Kormendy, J. & Kennicutt, R.C. 2004, ARAA, 42, 603

Krick, J.E. et al. 2011, ApJ, 735, 76

Larson, R.B. et al. 1980, ApJ, 237, 692

Lawrence, A. et al. 2007, MNRAS, 379, 1599

Martínez-Delgado, D. et al. 2009, ApJ, 692, 955

Martínez-Delgado, D. et al. 2010, AJ, 140, 962

Martínez-Delgado, D. et al. 2012, ApJL, 748, L24

Mihos, J.C. 1995, ApJL, 438, L75

Mihos, J.C. et al. 2005, ApJL, 631, L41

Moore, B. et al. 1996, Nature, 379, 613

Moster, B. P., Macciò, A. V., Somerville, R. S., Naab, T., & Cox, T. J. 2011, MNRAS, 415, 3750

Muñoz-Mateos, J.C. et al. 2009, ApJ, 701, 1965

Muratov, A. L., & Gnedin, O. Y. 2010, ApJ, 718, 1266
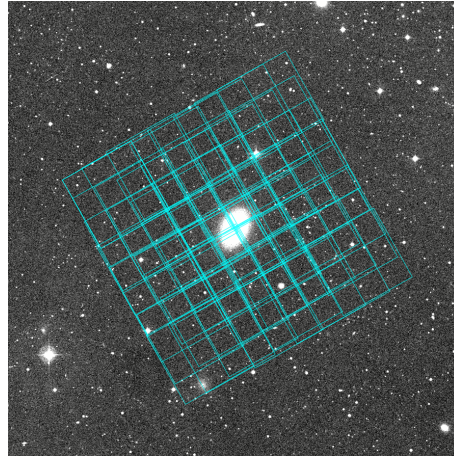
Figure 4: An example IRAC AOR footprint overlaid on a $30' \times 30'$ DSS image of NGC4531. The $10'$ mosaic "core" (1800 s per sky position) is 3.5 times the $2.86'$ D_{25} diameter for this galaxy (see § 1.2.2); including the 1200 s-deep inner periphery of the mosaic, the linear extent of the map is 4.7 times the galaxy diameter.

Naab, T., & Burkert, A. 2003, ApJ, 597, 893

Naab, T., Khochfar, S., & Burkert, A. 2006, ApJL, 636, L81

Nipoti, C., Londrillo, P., & Ciotti, L. 2003, MNRAS, 342, 501

Padmanabhan, N. et al. 2008, ApJ, 674, 1217

Pahre, M.A., Ashby, M.L.N., Fazio, G.G., & Willner, S.P. 2005, ApJS, 154, 235

Peñarrubia, J. et al. 2005, ApJ, 626, 128

Poggianti, B.M. et al. 2006, ApJ, 642, 188

Postman, M. 2005, ApJ, 623, 721

Press, W.H. et al. 2007, Numerical Recipes: The Art of Scientific Computing, Third Edition

Quilis, V., Moore, B., & Bower, R. 2000, Science, 288, 1617

Quinn, P. J. 1984, ApJ, 279, 596

Regan, M. et al. 2006, ApJ, 652, 1112

Rudick, C.S. et al. 2010, 720, 569

Schweizer, F. 1980, ApJ, 237, 303

Schweizer, F. 1982, ApJ, 252, 455

Sheth, K. et al. 2010, PASP, 122, 1397

Skrutskie, M.F. et al. 2006, AJ, 131, 1163

Smith, G.P. et al. 2005, ApJ, 620, 78

Spitler, L.R., Forbes, D.A., & Beasley, M.A. 2008, MNRAS, 389, 1150

Springel, V., & White, S. D. M. 1999, MNRAS, 307, 162

Tal, T. et al. 2009, ApJ, 138, 1417

Teyssier, R., Chapon, D., & Bournaud, F. 2010, ApJL, 720, L149

Toomre, A., & Toomre, J. 1972, ApJ, 178, 623

Tully, R.B. et al. 2009, AJ, 138, 323

van Dokkum, P. et al. 2005, ApJ, 130, 2647

Wang, J., Hammer, F., Athanassoula, E., et al. 2012, A&A, 538, A121

White, S. D. M. 1978, MNRAS, 184, 185

White, S. D. M. 1979, MNRAS, 189, 831

Wilman, D.J. et al. 2009, 692, 298

Wright, E. et al. 2010, AJ, 140, 1882

Yoon, S.-J., Yi, S. K., & Lee, Y.-W. 2006, Science, 311, 1129

2   Scheduling Profile

Every AOR is visible for two windows during the Cycle 10 time period, with each window spanning ∼40–60 days, as shown in Figure 5 below. Figure 5 also shows the distribution of the sources on the sky. The proposed program has no timing constraints which should enhance its "schedulability".
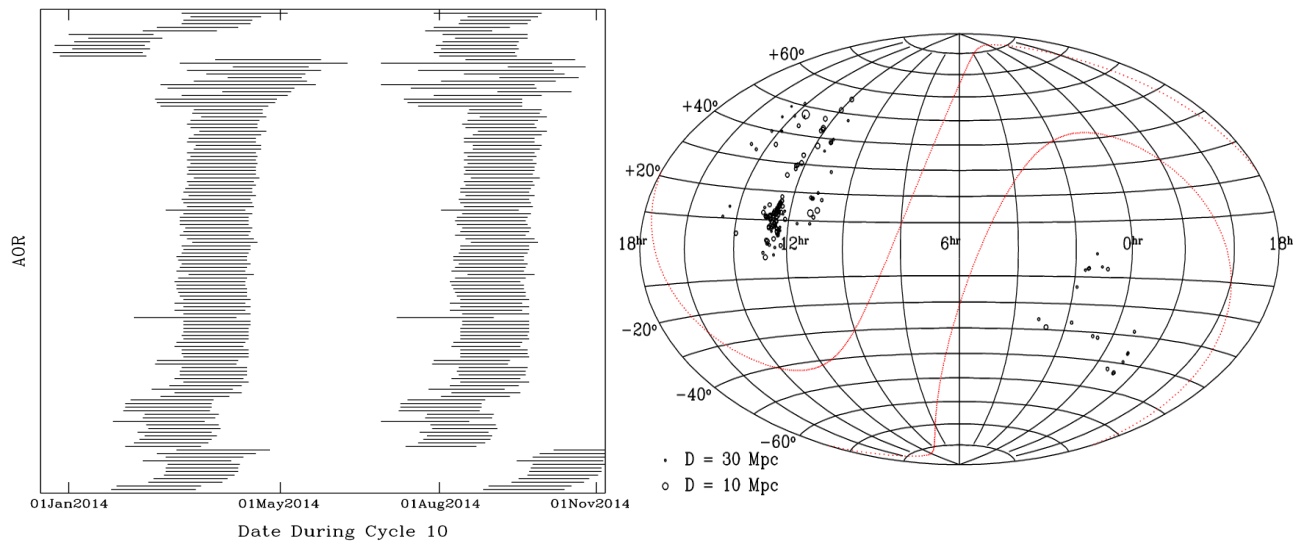
Figure 5: *Left*: A representation of the visibility windows for each AOR. Each AOR has two windows that span ∼40–60 days each. The x-axis spans the Cycle 10 period whereas the y-axis shows each AOR. *Right*: The distribution of the sources on the sky in Equatorial coordinates. The red dotted lines show the Milk Way "Zone of Avoidance" ($|b| < 20°$). Most of the early-type galaxies reside in or near the Virgo Cluster (see also Figure 1) with RA ∼11–15 hrs.

3 Brief Team Resume

Daniel A. Dale (Wyoming) is an expert on studies of star formation from low- to intermediate-redshift, as well as on the infrared spectra and panchromatic broadband spectral energy distributions of normal galaxies. He has extensive experience with *Spitzer* observations and data processing as a CoI on the SINGS, LVL, and 5MUSES legacy programs and as a CoI on the three Cycles 6 and 8 projects described in the next section.

Kate L. Barnes (Indiana) is in her second year of postdoctoral work. Her Ph.D. dissertation examined star formation rate indicators in the outer edges of spiral galaxies. She is PI on a Cycle 6 study of the extended disk in M 83 as well as CoI on two additional Warm Mission programs described in the next section.

Robert Feldmann (Berkeley) is a Hubble Fellow who specializes in numerical models of the formation of galaxies over cosmic time, covering topics that include tracking the merger history of elliptical galaxies and understanding the Kennicutt-Schmidt law in star-forming galaxies.

Shawn M. Staudaher (Wyoming) finished his third year of graduate school and his thesis focuses on our Cycle 8 project described in the following section. He spent two years before graduate school as a post-baccalaureate research assistant with Dale. He has led the IRAC data processing and mosaic construction for the Cycle 8 and two Cycle 6 programs described in the following section.

Liese van Zee (Indiana) is an expert on galaxy formation and evolution with an emphasis on investigating the links between star formation, elemental enrichment, and gas distribution and kinematics in star-forming galaxies. She has extensive experience working with multi-wavelength data sets (UV, optical, IR, and radio). She is PI of a program in both Cycle 6 and Cycle 8, as described in the following section, and is CoI on LVL.

Selected Related Publications
Star Formation in the Outer Disks of Spiral Galaxies: Ultraviolet and Hα Photometry
    Barnes et al. 2011, ApJ, 743, 137
Star Formation in the Outer Disk of Spiral Galaxies
    Barnes et al. 2012, ApJ, 757, 64
An Ultraviolet-to-Radio Broadband Spectral Atlas of Nearby Galaxies
    Dale et al. 2007, ApJ, 655, 863
Herschel Far-IR and Submm Photometry for the KINGFISH Sample of Nearby Galaxies
    Dale et al. 2012, ApJ, 745, 95
The *Spitzer* Local Volume Legacy: Survey Description and Infrared Photometry
    Dale et al. 2009, ApJ, 703, 517
Tidal Debris in Elliptical Galaxies as Tracers of Mergers with Disks
    Feldmann et al. 2008, ApJ, 684, 1062
The Hubble Sequence in Groups: The Birth of the Early-type Galaxies
    Feldmann et al. 2011, ApJ, 736, 88
Rotationally Supported Virgo Cluster Dwarf Elliptical Galaxies: Stripped Dwarf Irregular Galaxies?
    van Zee et al. 2004, AJ, 128, 121
Stellar Populations of Dwarf Elliptical Galaxies: UBVRI Photometry of Dwarf Elliptical Galaxies in the Virgo Cluster
    van Zee et al. 2004, AJ, 128, 2797

4   Summary of Existing Programs

Kate Barnes is the PI of 60116, a 30.2-hour Cycle 6 Warm Mission program to probe the extended older stellar population in M 83. The data have been post-pipeline processed, and we have optimized the creation of their image mosaics, developed routines for masking foreground stars and background galaxies, extracted surface brightness profiles, and compared the radial extent of the older population to the Hɪ radius. The results appeared in her recently completed dissertation, and a manuscript is in preparation.

Liese van Zee is the PI of 60094, a 69.7-hour Cycle 6 Warm Mission program to probe the older stellar population in the outskirts of galaxies with extended Hɪ disks. The observations for this program were completed in August 2010. The data have been post-pipeline processed, and we have optimized the creation of their image mosaics, developed routines for masking foreground stars and background galaxies, extracted surface brightness profiles, and compared the radial extent of the older population to the Hɪ radius. Results are included in this proposal. van Zee is also PI of 80025, a 1005.3-hour Cycle 8 program to map the extended disks in a sample of normal galaxies. All of the AORs have been observed and the data have been post-pipeline processed into science-ready mosaics. Analysis is underway on optimal foreground star subtraction and faint outer disk detection. Separate manuscripts for first papers on two individual galaxies are in progress.

Daniel Dale is Technical Contact for the above programs led by Barnes and van Zee. Dale is leading the data processing efforts on these programs.

5 Observation Summary Table

Galaxy	Galaxy	K_s (mag)	cz (km/s)	T	Position (J2000)	# grid points	AOR (hr)
PGC 02053	NGC0148	9.12	1516	-1	00h34m15.50s$-$31d47m09.6s	7$\times$ 7	3.1
PGC 02778	NGC0254	8.82	1629	0	00h47m27.61s$-$31d25m18.3s	7$\times$ 7	3.1
PGC 02980	NGC0274	9.40	1750	-3	00h51m01.86s$-$07d03m25.0s	6$\times$ 6	2.3
PGC 03768	NGC0357	8.57	2406	0	01h03m21.88s$-$06d20m21.2s	8$\times$ 8	4.1
PGC 04524	NGC0448	9.40	1917	-2	01h15m16.52s$-$01d37m34.3s	6$\times$ 6	2.3
PGC 05663	NGC0584	7.43	1872	-5	01h31m20.75s$-$06d52m05.0s	12$\times$12	9.0
PGC 05766	NGC0596	8.06	1876	-5	01h32m52.08s$-$07d01m54.6s	8$\times$ 8	4.1
PGC 06110	NGC0636	8.53	1805	-5	01h39m06.53s$-$07d30m45.4s	7$\times$ 7	3.1
PGC 06598	IC01729	9.75	1495	-3	01h47m55.26s$-$26d53m31.7s	6$\times$ 6	2.3
PGC 06983	NGC0720	7.39	1722	-5	01h53m00.50s$-$13d44m19.2s	13$\times$13	10.6
PGC 10330	NGC1079	8.45	1447	0	02h43m44.34s$-$29d00m12.1s	8$\times$ 8	4.1
PGC 771919	NGC1201	7.73	1720	-2	03h04m07.98s$-$26d04m10.7s	10$\times$10	6.3
PGC 32533	NGC3414	8.07	1414	-1	10h51m16.21s+27d58m30.4s	8$\times$ 8	4.1
PGC 32787	NGC3457	9.69	1158	-5	10h54m48.63s+17d37m16.5s	6$\times$ 6	2.3
PGC 33160	NGC3489	7.42	690	-2	11h00m18.57s+13d54m04.4s	9$\times$ 9	5.1
PGC 33604	NGC3524	9.68	1321	0	11h06m32.10s+11d23m07.5s	6$\times$ 6	2.3
PGC 33615	NGC3522	10.49	1221	-5	11h06m40.46s+20d05m08.0s	6$\times$ 6	2.3
PGC 34107	IC00676	9.92	1402	-1	11h12m39.82s+09d03m21.0s	6$\times$ 6	2.3
PGC 34257	NGC3593	7.55	627	0	11h14m37.00s+12d49m03.6s	16$\times$16	16.0
PGC 34325	NGC3595	9.52	2186	-1	11h15m25.55s+47d26m49.3s	6$\times$ 6	2.3
PGC 34326	NGC3599	9.48	755	-3	11h15m26.96s+18d06m37.4s	6$\times$ 6	2.3
PGC 34426	NGC3607	7.11	951	-4	11h16m54.64s+18d03m06.3s	13$\times$13	10.6
PGC 34684	NGC3626	8.24	1493	0	11h20m03.81s+18d21m24.6s	8$\times$ 8	4.1
PGC 34908	NGC3648	9.54	1988	-4	11h22m31.51s+39d52m36.8s	6$\times$ 6	2.3
PGC 35003	NGC3658	9.25	2044	-4	11h23m58.26s+38d33m44.4s	6$\times$ 6	2.3
PGC 35064	NGC3665	7.74	2080	-4	11h24m43.67s+38d45m46.3s	9$\times$ 9	5.1
PGC 35352	NGC3694	10.51	2279	-4	11h28m54.13s+35d24m50.4s	6$\times$ 6	2.3
PGC 36205	IC00719	9.71	1860	-2	11h40m18.51s+09d00m35.6s	6$\times$ 6	2.3
PGC 38527	NGC4124	8.69	1679	-1	12h08m09.62s+10d22m44.0s	13$\times$13	10.6
PGC 38742	NGC4150	9.05	226	-4	12h10m33.65s+30d24m05.5s	6$\times$ 6	2.3
PGC 38890	NGC4168	8.55	2215	-5	12h12m17.27s+13d12m18.7s	7$\times$ 7	3.1
PGC1190620	NGC4179	7.94	1228	-2	12h12m52.11s+01d17m58.9s	9$\times$ 9	5.1
PGC 39124	NGC4200	10.46	2376	-3	12h14m44.23s+12d10m50.7s	6$\times$ 6	2.3
PGC 39251	NGC4215	9.11	2067	-1	12h15m54.54s+06d24m04.1s	7$\times$ 7	3.1
PGC 39384	NGC4233	8.86	2371	-1	12h17m07.68s+07d37m27.8s	7$\times$ 7	3.1
PGC 39412	NGC4241	9.18	2235	0	12h17m59.90s+06d39m15.1s	7$\times$ 7	3.1
PGC 39437	NGC4245	8.41	815	0	12h17m36.77s+29d36m28.8s	8$\times$ 8	4.1
PGC 39492	NGC4251	7.79	1067	-1	12h18m08.25s+28d10m31.4s	9$\times$ 9	5.1
PGC 39592	NGC4255	9.56	1955	-2	12h18m56.15s+04d47m10.1s	6$\times$ 6	2.3
PGC 39657	NGC4259	10.74	2492	-2	12h19m22.21s+05d22m35.0s	6$\times$ 6	2.3
PGC 39659	NGC4261	7.40	2238	-5	12h19m23.22s+05d49m30.8s	12$\times$12	9.0
PGC 39676	NGC4262	8.40	1359	-2	12h19m30.57s+14d52m39.6s	6$\times$ 6	2.3

PGC 39710	NGC4267	7.92	1001	−4	12h19m45.24s+12d47m53.8s	8× 8	4.1
PGC 39712	NGC4268	9.55	2060	0	12h19m47.22s+05d17m01.6s	6× 6	2.3
PGC 39719	NGC4269	10.02	2074	−2	12h19m49.19s+06d00m53.9s	6× 6	2.3
PGC 39718	NGC4270	9.12	2357	−2	12h19m49.47s+05d27m48.4s	7× 7	3.1
PGC 39759	NGC4277	10.84	2499	0	12h20m03.72s+05d20m28.9s	6× 6	2.3
PGC 39764	NGC4278	7.26	648	−5	12h20m06.82s+29d16m50.7s	12×12	9.0
PGC 39922	NGC4292	9.71	2258	−2	12h21m16.46s+04d35m44.5s	6× 6	2.3
PGC 40179	NGC4324	8.54	1667	−1	12h23m06.18s+05d15m01.2s	7× 7	3.1
PGC 40228	NGC4346	8.24	762	−2	12h23m27.94s+46d59m37.8s	9× 9	5.1
PGC 40240	NGC4339	8.62	1289	−5	12h23m34.95s+06d04m54.3s	7× 7	3.1
PGC 40245	NGC4340	8.42	932	0	12h23m35.29s+16d43m20.5s	8× 8	4.1
PGC 40252	NGC4342	9.04	751	−3	12h23m39.00s+07d03m14.4s	6× 6	2.3
PGC 40295	NGC4350	7.85	1247	−1	12h23m57.87s+16d41m36.3s	9× 9	5.1
PGC 40375	NGC4365	6.79	1240	−5	12h24m28.28s+07d19m03.6s	15×15	14.0
PGC 40442	NGC4371	7.80	941	−1	12h24m55.43s+11d42m15.2s	9× 9	5.1
PGC 40455	NGC4374	6.33	910	−5	12h25m03.74s+12d53m13.1s	16×16	16.0
PGC 40476	NGC4377	8.88	1375	−3	12h25m12.34s+14d45m43.8s	6× 6	2.3
PGC 40484	NGC4379	8.86	1071	−3	12h25m14.74s+15d36m26.9s	6× 6	2.3
PGC 40515	NGC4382	6.25	758	−1	12h25m24.11s+18d11m29.4s	17×17	18.0
PGC 40562	NGC4387	9.22	472	−5	12h25m41.68s+12d48m37.9s	6× 6	2.3
PGC 40564	NGC4385	9.97	2140	−1	12h25m42.80s+00d34m21.4s	6× 6	2.3
PGC 40643	NGC4405	9.49	1747	0	12h26m07.15s+16d10m51.6s	6× 6	2.3
PGC 40653	NGC4406	6.27	-221	−5	12h26m11.74s+12d56m46.4s	17×17	18.0
PGC 40756	NGC4417	8.23	843	−2	12h26m50.61s+09d35m03.3s	9× 9	5.1
PGC 40772	NGC4419	7.78	-261	0	12h26m56.44s+15d02m50.6s	10×10	6.3
PGC 40785	NGC4421	8.94	1517	−1	12h27m02.54s+15d27m41.3s	8× 8	4.1
PGC 40850	NGC4429	6.87	913	−1	12h27m26.51s+11d06m27.8s	16×16	16.0
PGC 40886	NGC4434	9.30	1068	−5	12h27m36.68s+08d09m15.6s	6× 6	2.3
PGC 40950	NGC4442	7.37	515	−2	12h28m03.88s+09d48m13.4s	13×13	10.6
PGC 41083	NGC4454	9.23	2407	0	12h28m50.75s−01d56m21.1s	7× 7	3.1
PGC 41101	NGC4457	7.84	881	0	12h28m59.01s+03d34m14.1s	8× 8	4.1
PGC 41104	NGC4459	7.20	1215	−4	12h29m00.01s+13d58m42.1s	10×10	6.3
PGC 41164	NGC4469	8.14	498	0	12h29m28.03s+08d44m59.7s	10×10	6.3
PGC 41220	NGC4472	5.50	997	−5	12h29m46.76s+08d00m01.7s	17×17	18.0
PGC 41228	NGC4473	7.26	2236	−5	12h29m48.87s+13d25m45.7s	13×13	10.6
PGC 41241	NGC4474	8.78	1624	−2	12h29m53.55s+14d04m06.9s	7× 7	3.1
PGC 41260	NGC4477	7.35	1355	−2	12h30m02.20s+13d38m11.8s	11×11	7.6
PGC 41339	NGC4483	9.39	881	0	12h30m40.65s+09d00m56.4s	6× 6	2.3
PGC 41361	NGC4486	5.90	1307	−4	12h30m49.42s+12d23m28.0s	17×17	18.0
PGC 41441	NGC4494	7.14	1350	−5	12h31m24.10s+25d46m30.9s	14×14	12.2
PGC 41772	NGC4526	6.54	603	−2	12h34m03.09s+07d41m58.3s	17×17	18.0
PGC 41781	NGC4528	9.02	1374	−3	12h34m06.07s+11d19m16.5s	6× 6	2.3
PGC 41806	NGC4531	8.89	107	−2	12h34m15.89s+13d04m31.2s	8× 8	4.1
PGC 41923	NGC4543	10.71	2399	−5	12h35m20.24s+06d06m54.3s	6× 6	2.3
PGC 41943	NGC4550	8.74	381	−2	12h35m30.58s+12d13m15.0s	8× 8	4.1
PGC 41968	NGC4552	6.84	322	−5	12h35m39.81s+12d33m22.8s	15×15	14.0
PGC 42051	NGC4564	7.98	1142	−5	12h36m26.98s+11d26m21.4s	9× 9	5.1

PGC 42096	NGC4570	7.76	1750	−2	12h36m53.40s+07d14m47.9s	10×10	6.3
PGC 42149	NGC4578	8.51	2284	−2	12h37m30.56s+09d33m18.3s	8× 8	4.1
PGC 42199	NGC4581	9.72	1818	−4	12h38m05.17s+01d28m39.9s	6× 6	2.3
PGC 42401	NGC4596	7.53	1870	−1	12h39m55.95s+10d10m34.1s	11×11	7.6
PGC 42427	NGC4598	10.26	1961	−2	12h40m11.93s+08d23m01.5s	7× 7	3.1
PGC 42545	NGC4608	8.24	1864	−2	12h41m13.29s+10d09m20.4s	9× 9	5.1
PGC 42574	NGC4612	8.66	1884	−2	12h41m32.75s+07d18m53.6s	7× 7	3.1
PGC 42628	NGC4621	6.86	444	−5	12h42m02.24s+11d38m49.3s	15×15	14.0
PGC 42647	NGC4623	9.56	1892	−1	12h42m10.69s+07d40m37.0s	7× 7	3.1
PGC 42728	NGC4638	8.24	1148	−3	12h42m47.42s+11d26m33.0s	7× 7	3.1
PGC 42734	NGC4636	6.62	1094	−5	12h42m49.83s+02d41m16.0s	17×17	18.0
PGC 42797	NGC4643	7.46	1319	0	12h43m20.14s+01d58m41.8s	10×10	6.3
PGC 42831	NGC4649	5.82	1095	−5	12h43m39.98s+11d33m09.7s	17×17	18.0
PGC 42917	NGC4660	8.23	1083	−5	12h44m31.98s+11d11m25.9s	7× 7	3.1
PGC 42970	NGC4665	7.51	785	0	12h45m05.99s+03d03m20.8s	11×11	7.6
PGC 43149	NGC4684	8.45	1589	−1	12h47m17.52s−02d43m38.7s	8× 8	4.1
PGC 43241	NGC4694	9.10	1175	−2	12h48m15.08s+10d59m01.0s	7× 7	3.1
PGC 43375	NGC4710	7.66	1129	0	12h49m38.83s+15d09m55.6s	14×14	12.2
PGC 43516	NGC4733	9.20	905	−3	12h51m06.78s+10d54m43.5s	7× 7	3.1
PGC 43671	NGC4753	6.82	1396	0	12h52m22.11s−01d11m58.9s	16×16	16.0
PGC 43733	NGC4762	7.44	1006	−2	12h52m56.05s+11d13m50.9s	17×17	18.0
PGC 44600	NGC4866	7.99	1988	−1	12h59m27.14s+14d10m15.8s	12×12	9.0
PGC 44719	NGC4880	9.54	1470	0	13h00m10.57s+12d28m59.9s	9× 9	5.1
PGC 46552	NGC5103	9.56	1283	−2	13h20m30.08s+43d05m02.3s	6× 6	2.3
PGC 47257	NGC5173	10.13	2419	−5	13h28m25.27s+46d35m29.9s	6× 6	2.3
PGC 47413	NGC5195	6.39	464	0	13h29m59.59s+47d15m58.1s	17×17	18.0
PGC 49356	NGC5353	7.65	2165	0	13h53m26.69s+40d16m58.9s	10×10	6.3
PGC 49380	NGC5355	10.57	2408	−2	13h53m45.56s+40d20m19.2s	6× 6	2.3
PGC 49547	NGC5363	6.98	1138	0	13h56m07.21s+05d15m17.2s	11×11	7.6
PGC 49608		10.35	2133	0	13h56m57.93s+46d01m46.2s	6× 6	2.3
PGC 50331	NGC5481	9.56	2004	−3	14h06m41.27s+50d43m24.0s	6× 6	2.3
PGC 51251	NGC5582	9.07	1435	−5	14h20m43.12s+39d41m36.9s	7× 7	3.1
PGC 51332	NGC5587	9.76	2303	0	14h22m10.71s+13d55m05.0s	6× 6	2.3
PGC 51431	NGC5611	9.84	1957	−1	14h24m04.78s+33d02m50.6s	6× 6	2.3
PGC 51753		11.13	2382	0	14h29m12.88s+44d50m33.2s	6× 6	2.3
PGC 51995	NGC5666	10.20	2221	−6	14h33m09.21s+10d30m38.9s	6× 6	2.3
PGC 52154	NGC5689	8.45	2160	0	14h35m29.69s+48d44m29.9s	8× 8	4.1
PGC 52741		10.29	1692	−1	14h46m20.38s+34d24m20.9s	6× 6	2.3
PGC 69964	NGC7404	10.18	1899	−3	22h54m18.61s−39d18m53.8s	6× 6	2.3
PGC 70085	IC05267B	10.17	1663	−2	22h56m57.16s−43d45m36.7s	6× 6	2.3
PGC 70090	IC01459	6.92	1659	−5	22h57m10.61s−36d27m44.0s	14×14	12.2
PGC 70094	IC05267	7.60	1713	−2	22h57m13.57s−43d23m46.1s	13×13	10.6
PGC 70110	IC05269	9.55	1967	−2	22h57m43.66s−36d01m34.4s	7× 7	3.1
PGC 70676	NGC7507	7.33	1536	−5	23h12m07.59s−28d32m22.6s	9× 9	5.1
PGC 71213	NGC7632	9.25	1531	−3	23h22m00.90s−42d28m49.8s	6× 6	2.3

There are 777.7 hrs total requested for this observing program.

6 Modification of the Proprietary Period

No modification to the proprietary period is requested for this program. We are submitting final AORs for this program.

7 Summary of Duplicate Observations

No duplicate observations are proposed. A search of the ROC for all 155 early-type galaxies described in Section 1.2.1 reveals 12 duplications. Therefore observations for these 12 galaxies are not included in this proposal (but their archival data would be included in the final analysis). In addition, IRAC 3.6 μm data for 99 of the remaining 143 galaxies exist in the ROC. However, none of these observations represent a formal duplication (at least 1/4 of the proposed integration over at least 1/4 of the proposed spatial coverage). A typical example is NGC 4531 (PGC 41806) which was observed under the auspices of the S^{4}G program (PI K. Sheth). The effective S^{4}G integration is 240 s per position on the sky over a single IRAC field-of-view covering ~ 25 arcmin^2. In contrast, our proposed areal coverage is 4 times larger for the core region (1800 s per position on the sky; Figure 4) and 7.1 times larger if the inner periphery region is included (at 1200 s per position on the sky).

8 Summary of Scheduling Constraints/ToOs

There are no scheduling constraints or ToOs in this program.